

## Progress in Simulating/Realisation SESANS in Time-of-Flight Mode at Pulsed and Stationary Neutron Sources

Kraan, W. H.; Akselrod, L. A.; Yashina, E. G.; Sumbatyan, A. A.; Grigoriev, S. V.

**DOI**

[10.1134/S1027451020070253](https://doi.org/10.1134/S1027451020070253)

**Publication date**

2020

**Document Version**

Final published version

**Published in**

Journal of Surface Investigation

**Citation (APA)**

Kraan, W. H., Akselrod, L. A., Yashina, E. G., Sumbatyan, A. A., & Grigoriev, S. V. (2020). Progress in Simulating/Realisation SESANS in Time-of-Flight Mode at Pulsed and Stationary Neutron Sources. *Journal of Surface Investigation*, 14, S108-S116. <https://doi.org/10.1134/S1027451020070253>

**Important note**

To cite this publication, please use the final published version (if applicable). Please check the document version above.

**Copyright**

Other than for strictly personal use, it is not permitted to download, forward or distribute the text or part of it, without the consent of the author(s) and/or copyright holder(s), unless the work is under an open content license such as Creative Commons.

**Takedown policy**

Please contact us and provide details if you believe this document breaches copyrights. We will remove access to the work immediately and investigate your claim.

# Progress in Simulating/Realisation SESANS in Time-of-Flight Mode at Pulsed and Stationary Neutron Sources

W. H. Kraan<sup>a, \*</sup>, L. A. Akselrod<sup>b</sup>, E. G. Yashina<sup>b</sup>, A. A. Sumbatyan<sup>b</sup>, and S. V. Grigoriev<sup>b</sup>

<sup>a</sup>Delft University of Technology, JB Delft, 2629 The Netherlands

<sup>b</sup>Petersburg Nuclear Physics Institute, National Research Center “Kurchatov Institute,” Gatchina, Leningrad oblast, 188300 Russia

\*e-mail: W.H.Kraan@gmail.com

Received June 27, 2019; revised August 27, 2019; accepted August 29, 2019

**Abstract**—We created software to simulate the Larmor precession in a setup for SESANS with adiabatic/radio frequency flippers in magnets designed to measure the time-of-flight on pulsed or stationary neutron sources. The values and spatial configurations of the magnetic fields of the existing prototype magnets we used as input data. For an empty setup, we calculate the polarization of a “divergent ribbon beam” 2 cm high, depending on the neutron wavelength  $\lambda$ . In the “scattering experiment”, we show how to convert  $\lambda$  to the “spin-echo length”  $\delta$ . For  $\lambda = 10 \text{ \AA}$ , flippers at a distance of 140 cm and a radio frequency 1 MHz we find  $\delta \approx 10 \text{ }\mu\text{m}$ . Extension to  $\delta = 20 \text{ }\mu\text{m}$  is realistic.

**Keywords:** Larmor precession, matrix multiplication, small angle neutron scattering

**DOI:** 10.1134/S1027451020070253

## INTRODUCTION

SESANS is a method of spin-echo small-angle neutron scattering with the transfer of wave vector  $Q \sim 10^{-6} - 10^{-3} \text{ nm}^{-1}$  in regions with magnetic field  $\mathbf{B}$  in the form of parallelograms with a “device angle”  $\theta_0 < 90^\circ$  (Fig. 1). Depolarization of the beam due to scattering in a sample with an inhomogeneous density is measured as a function of the parameter of the spin-echo length  $\delta$ , which is specified by the “technical” parameters of the setup: neutron wavelength  $\lambda$ , magnetic induction  $\mathbf{B}$ , and length. SESANS is used in materials science in samples with inhomogeneities of  $10^2 - 10^4 \text{ nm}$ . Examples are phase transitions, defects, porosity, clusters, biological nanostructures, membranes, colloids, ferromagnetic domains, etc. [1–7].

Neutrons with a wavelength  $\lambda$  flying along a path of length  $L$  through a uniform magnetic field with induction  $\mathbf{B}$  “collect” the precession phase  $\varphi = cLB\lambda$  [1]. According to this rule, for field regions in the form of a parallelogram, it can be found that the precession phases  $\varphi_i$  in the arm 1 of the neutron spin-echo (NSE) before ( $i = 1$ ) and arm 2 ( $i = 2$ ) after scattering in the sample, while the neutron crosses the field, are:

$$\varphi_i = \lambda(LB + \Gamma\psi_i) \quad (i = 1, 2), \quad (1)$$

where the constant  $c = 4\pi\mu_n/h^2 = 4.632 \times 10^{14} \text{ T}^{-1} \text{ m}^{-2}$ ,  $\mu_n$ ,  $m_n$ ,  $h$  are neutron mass, magnetic moment and Planck constant, respectively,  $\psi_i$  are the angles between the  $x$  axis and the flight directions in the NSE

arms.  $\lambda\Gamma\psi_i$  in (1) is the angle labeling term. For a rectangular field, it is zero in the first order.  $\Gamma$  is called “labeling coefficient”.

Suppose that a neutron is scattered by  $\psi_2 - \psi_1 = \theta_s$  in the  $y$  direction (Fig. 1a). Then (1) gives an offset from NSE due to this process:  $\varphi_1 - \varphi_2 = \Gamma\theta_s$ . It has a wave vector transfer  $Q_y = (4\pi/\lambda)\sin(\theta_s/2)$ . If we divide the offset by  $Q_y$  (with  $\sin\theta_s = \theta_s$ ), we get the dimension length:

$$\delta = \lambda\Gamma\theta_s/Q_y, \quad (2)$$

called “spin-echo length”. It follows from (1) and (2) that  $\delta$  depends on  $\theta_s$ ,  $L$ ,  $B$ , and  $\lambda$ .

In the practice of a SESANS measurement, at a fixed  $\delta$ , the (damped) oscillating signal  $P(\delta, \Delta\varphi)$  after the analyzer is measured as a function of the precession phase  $\Delta\varphi$  collected in a “phase coil” in one NSE-arm to make extra offset from NSE. The polarization  $P(\delta)$  is the (maximum) amplitude of the signal  $P(\delta, \Delta\varphi)$ . Scanning  $\delta$  means repeating, varying one of the parameters  $\theta_0$ ,  $L$ ,  $B$ ,  $\lambda$  within the range that the setup allows. The polarization  $P(\delta)$  measured in this way contains information on the  $\Sigma$  and  $d\Sigma/d\Omega$  (total and differential macroscopic cross sections). It is connected with the so-called “SESANS correlation function”  $G(\delta)$  via [1]:

$$\begin{aligned} P(\delta)/P_0(\delta) &= \exp(\Sigma l[G(\delta) - 1]), \\ G(\delta) &= 1/(k_0^2\Sigma) \iint d\Sigma/d\Omega \cos(Q_y\delta) dQ_y dQ_z, \end{aligned} \quad (3)$$

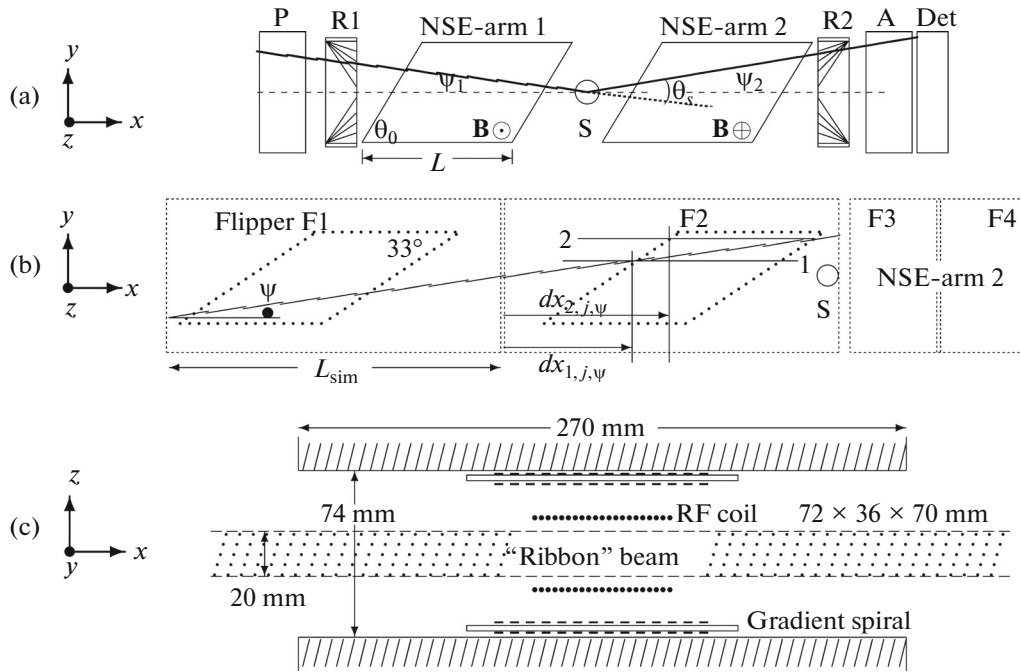


**Fig. 1.** (a) Principle of SESANS operation: P is a polarizer; A is an analyzer; R1/R2 are rotators to orient/analyze polarization vector along  $x$ ,  $y$  or  $z$  axes. The lines in R1/R2 suggest the “V-coils” to orient/analyze the polarization component parallel to  $y$ , i.e., perpendicular to the local field needed to observe the precession. (b) Top view of GATCHINA variant by calculating (17) the DC field profile along a horizontal trajectory through the flipper F2 ( $j = 2$ ) at  $\psi \neq 0$  (exaggerated). Sample S is located in a place with a small field in the NSE-arm 1. (c) Side view of one flipper with “gradient spirals” and RF-coil.

where  $l$  is the sample thickness,  $k_0 = 2\pi/\lambda$  is the neutron wave number,  $G(\delta)$  is a function decaying from unity at  $\delta = 0$ . A discussion of this is beyond the scope of this article; see [8] for more details.

The denominator  $P_0(\delta)$  is the polarization of the empty setup when “focused” on the spin-echo length  $\delta$  using the parameters  $\theta_s$ ,  $L$ ,  $B$ , and  $\lambda$ . Its value determines the quality and range of available  $\delta$  that are relevant for future users. If we take the parameter  $\lambda$  for scanning  $\delta$ , a complication may appear that  $d\Sigma/d\Omega$  changes with  $\lambda$ . By combining  $P(\delta)/P_0(\delta)$  measured varying  $\lambda$  at constant  $B$  with  $P(\delta)/P_0(\delta)$  measured varying  $B$  at constant  $\lambda$ , we can obtain additional information about the sample [8], which not available if, in the case of a monochromatic beam, only  $B$  is a variable parameter. In the case of a “white” beam and TOF mode, both options are available.

The purpose of the work was to find a realistic value for  $P_0(\delta)$  by simulating the precession in the SESANS variant with four “adiabatic RF/gradient-flippers” (RF – radio frequency) (Fig. 1b) in existing prototypes of electromagnets. We created software to simulate Larmor precession for a “beam” of trajectories. For input, we take data on magnetic fields much more accurate and complete than before [9]. We will simulate the offset from NSE after scattering in the “sample”. When applying (2), this will lead to accessible  $\delta$ .

Here we present the magnetic fields in our setup based on the latest field measurements/calculations; we give a simulation of the precession through a full setup, and not through one NSE-arm. Moreover, we discuss the consequence of imperfect setting of the polarization vector in the setup.

## MAGNETIC FIELDS IN THE SESANS SETUP

### DC Magnet

The component  $B_z^{DC}(x)$  of the DC electromagnet around the F1 flipper was measured in its real medium along its main axis to  $x = \pm 75$  cm. Fig. 2 shows the data ( $-40 < x < 70$ ) used for simulating the F1 flipper. The field of such a magnet is not uniform, but increases outside the plane  $z \equiv 0$  with  $z^2$ :

$$B_z^{DC}(x, z \neq 0) = B_z^{DC}(x, z = 0)[1 + \gamma_B(x)z^2]. \quad (4)$$

The coefficient  $\gamma_B(x)$  was measured between the poles; outside we describe  $B_z^{DC}(x, z \neq 0)$  with  $\gamma_B$  at the ends of the poles. The difference  $B_z^{DC}(x, z \neq 0) - B_z^{DC}(x, z = 0)$  is also shown in Fig. 2. If the field is configured so that the plateau reaches 34.3 mT, it does not exceed 0.6 mT.

In the plane  $z \equiv 0$  we measured the map  $B_z^{DC}(x, y)$  near one end of the polar gap. The contour line  $B_z^{DC}(x, y)$ ,

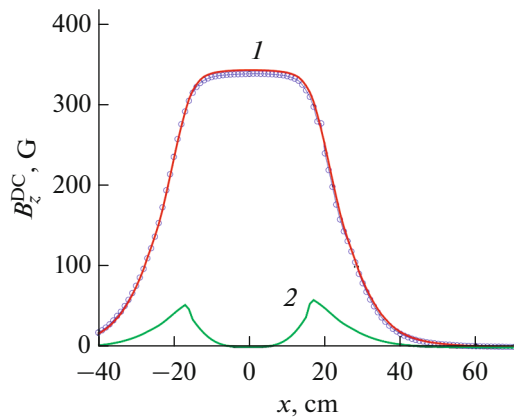


**Fig. 2.** Field  $B_z^{\text{DC}}(x)$  is measured (open circles) at  $\lambda = 2 \text{ \AA}$  along the axis of the DC magnet of F1 with  $33^\circ$ -poles. For simulation with  $\text{RF} = 1 \text{ MHz}$ , far from the axis ( $z = 1.0 \text{ cm}$ ),  $B_z^{\text{DC}}$  is symmetrized and adjusted so that the plateau  $34.32 \text{ mT}$  appears at  $\omega_{\text{RF}}/\gamma(I)$ . The increase in  $B_z^{\text{DC}}(x, z)$  from  $z = 0$  to  $z = 1$  is simulated using Eq. (4) (2). Multiplied by 10.

indicating the half plateau, repeats the shape of the poles ( $\theta_0 = 33.7^\circ \rightarrow \cot\theta_0 = 1.500$ ) in  $\Delta y$  by more than 2 cm around the axis. This indicates that the desired labelling coefficient  $\Gamma$  is indeed implemented for these poles.

#### Gradient and RF Field in Adiabatic/RF/Gradient Flipper

For gradient field, we applied spirals on both sides of the isolating plates and attached one plate directly to each magnet pole (Fig. 1c) in order to increase the field by two times compared to “isolated” mounting. The  $z$ -component of the field,  $B_z^{\text{GR}}$ , measured at  $\lambda = 4 \text{ \AA}$ , is shown in Fig. 3. Note that the component  $B_z^{\text{GR}}(x, z \equiv 0)$  is invariant over  $\Delta y = 20 \text{ mm}$ .

To create a RF field that is invariant over the equal  $y$ -range and keep this field “far” from the iron poles of the DC magnet, we introduce a rectangular coil  $\Delta y \times \Delta z = 72 \times 36 \text{ mm}$  with a length of 70 mm (Fig. 1c). Outside this coil, its field decays more slowly than the field of a square coil of the same height. This is useful for reducing the undesired components of  $P_{xz}$  and  $P_{yz}$  (third column in Fig. 4). We calculate the field strength  $\mathbf{H}^{\text{RF}}$  of this coil analytically based on the formula for the absolute value  $|\mathbf{H}|$  of the circular field of a finite section of wire. For each winding, the fields of the parts (top/bottom and side) are added. To obtain the field components  $H_z^{\text{RF}}(x_0)$  and  $H_x^{\text{RF}}(x_0)$  of the entire coil, the fields of all windings are added. The result ( $I = 2.5 \text{ A}$ ) is shown in Fig. 5b. We checked: the

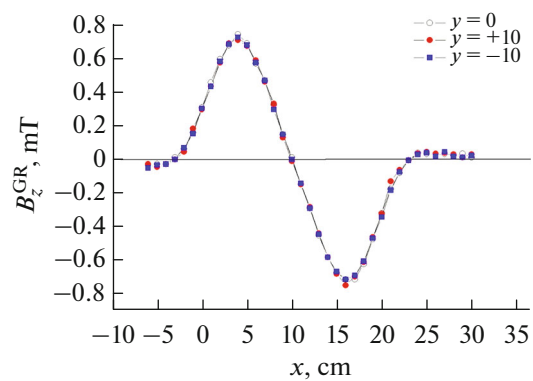


**Fig. 3.** The field generated by the gradient field spirals at both poles of the DC magnet (Fig. 1b), measured at  $\lambda = 4 \text{ \AA}$ .

$H_x^{\text{RF}}(x)$  component changes by less than 5% in the  $y$ -range of 20 mm; therefore, it is also “invariant”.

#### Guide Field and Current Screen

Around our prototype, we built two sets of coils with dimensions  $L_x \times L_y = 250 \times 50 \text{ cm}$  at a distance of  $d = 25 \text{ cm}$ , creating a vertical “guide field”  $\mathbf{G}$ . Again, for each coil, the field contributions of (long sides/ $x$  and start/end) are calculated analytically. The field  $G(x, y, z \equiv 0)$  around one NSE-arm is the sum of the fields of upper and lower coils. The line 1 in Fig. 6 is the sum of the  $z$ -components of the opposite fields of the coil sets around NSE-arm 1 and 2. The  $d/L_y$  ratio was 0.5: this is the “Helmholtz configuration” with the advantage that  $G(x, z)$  becomes very homogeneous near the beam axis. For  $|z| < 1 \text{ cm}$ ,  $|\mathbf{G}|$  deviation from  $G(x, z \equiv 0)$  over the entire length is less than 2 mA/cm. We must remember that the guide field between the poles of the DC magnets is “shielded”. This is taken into account by subtracting the profile in Fig. 2 weighted so that between the magnet poles the guide field  $G$  is suppressed by 95%. This is indicated in Fig. 6. We plan to install a “current screen” (a field calculated with the geometry in Fig. 1a) that creates a field step at  $x = 0$  to avoid a drift of the polarization vector to an undesirable direction during the transition from NSE-arm 1 to 2 (making the NSE experiment impossible).

## SIMULATING PRECESSION

### Matrix Multiplication

We identify the expected values of the spin components along  $x, y, z$  with the “polarization vector”  $\mathbf{P}(t)$ . In terms of this vector, the Larmor equation is usually written as follows:

$$d\mathbf{P}/dt = \gamma\mathbf{P}(t) \times \mathbf{B}, \quad (5)$$

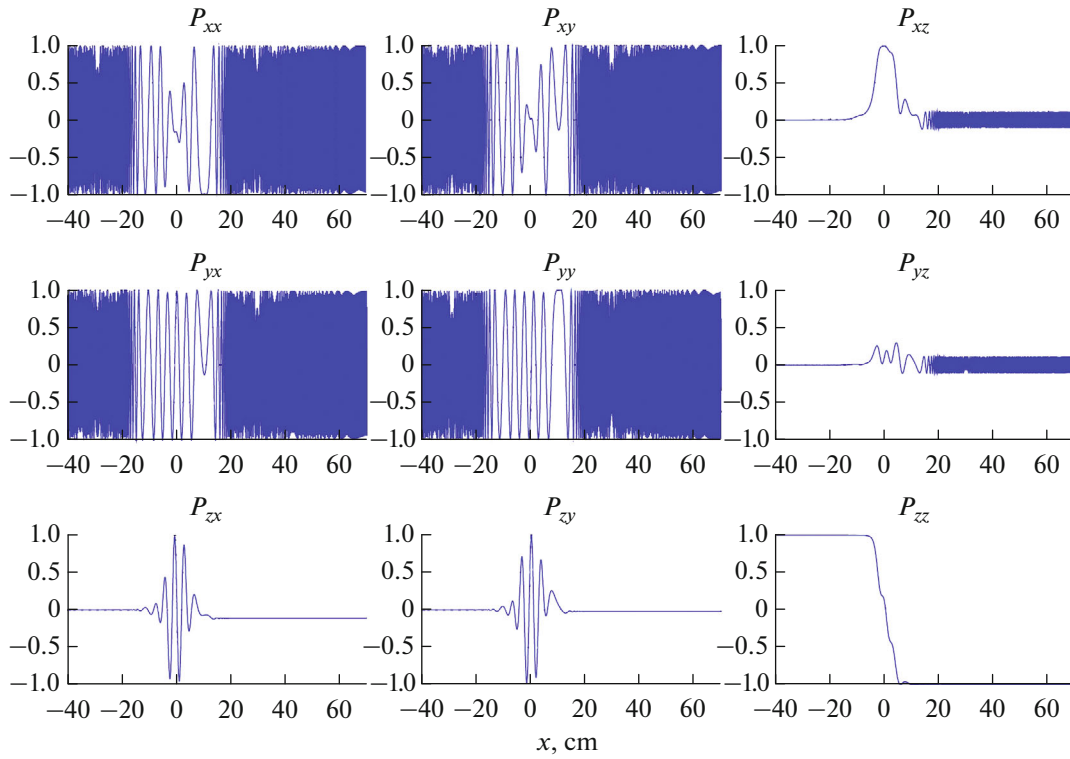


**Fig. 4.** The evolution of the vectors  $[(P_{xx}, P_{xy}, P_{xz}), (P_{yx}, P_{yy}, P_{yz}), (P_{zx}, P_{zy}, P_{zz})]$  in the flipper F1 (Fig. 1b) with parameters:  $\lambda = 4 \text{ \AA}$ ,  $z = 0.5$ ,  $\psi = 0$ ,  $\zeta = 0$ , plateau level is 343.3, number of simulation steps  $N = 2500$ .

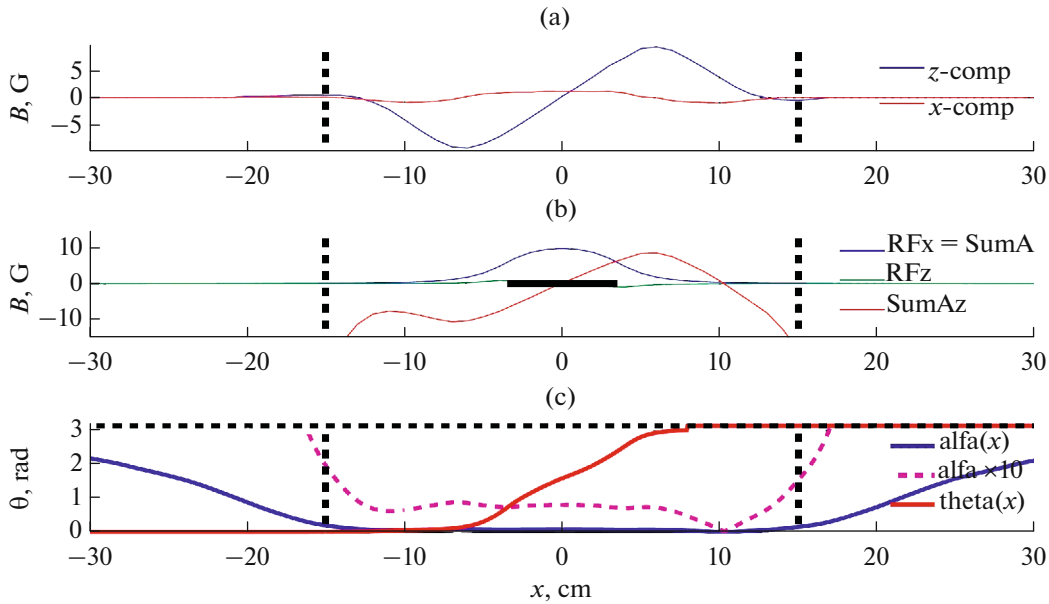


**Fig. 5.** Simulation input for the F1 flipper (Figs. 1b, 1c) (switched “ON”) according to Eqs. (7)–(11) ( $\lambda = 4 \text{ \AA}$ ,  $z = 0.5$ ,  $\psi = 0$ ,  $\zeta = 0$ ; number of simulation steps  $N = 2500$ ): (a) gradient field; (b) RF field; (c)  $\theta(x, z)$ .

with  $\gamma = 2\mu_n/\hbar$ . For a uniform magnetic field  $\mathbf{B}$  along  $z$ , this equation can be written as a standard  $(3 \times 3)$  matrix  $\mathbf{R}_z(\alpha)$  for rotation about  $z$ , where  $\alpha = \alpha(t) = \gamma|\mathbf{B}|t$  is the precession phase collected in time  $t$ , so that the field acts on the vector  $\mathbf{P}$ . For an arbitrary field  $\mathbf{B}$

(defined by polar angle  $\theta$  and azimuthal angle  $\phi$ ), Eq. (1) takes the form

$$P(t) = R_z(\phi)R_y(\theta)R_z(\alpha)R_y^{-1}(\theta)R_z^{-1}(\phi)P_{in}, \quad (6)$$

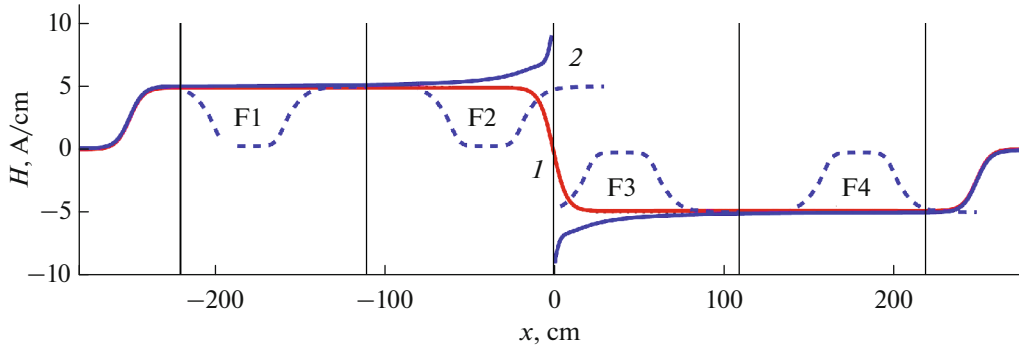


**Fig. 6.** Guide field component  $G_z(x, y=0, z \equiv 0)$  of two coil sets on the right with antiparallel field (1) and after adding the field of the current screen placed at  $x=0$  (2). The dotted parts represent the shielding of the guide field between the DC magnet poles. Vertical lines indicate a modular way of simulation.

where  $R_y$  is the standard  $(3 \times 3)$  matrix that describes rotation around  $y$ .

We use a “rotating coordinate system” [10, 11] around the  $z$  axis at the frequency  $\omega_{\text{RF}}$  of RF fields that are assumed to oscillate in phase. The advantage is that their time dependence is “transformed”, but with consequences: RF fields appear to be reduced by two times compared to their “DC-value”; a DC field  $B^* = \omega_{\text{RF}}/\gamma$  (with  $\gamma/(2\pi) = 2.9126 \text{ kHz/G}$ ) is subtracted; the longitudinal DC field components rotate at  $-\omega_{\text{RF}}$  around  $z$ : inefficiently, hence, they are ignored. The remaining field profiles  $\Sigma A_x$  and  $\Sigma A_z$  (near the beam:  $|y|, |z| < 1 \text{ cm}$ ) in the flippers are:

$$\Sigma A_z = \mu_0 H_z^{\text{GR}}(x, z) + B_z^{\text{DC}}(x, z) - B^* \quad (7)$$

(sum transverse comp),

$$\Sigma A_x = \mu_0 H_x^{\text{RF}}(x, z) \quad (\text{sum longitudinal comp}), \quad (8)$$

$\Sigma A_y$  is set to zero by selecting the initial phase of the ROT system. This means that  $\varphi = 0$  in (7).

The components  $\Sigma A_x$  and  $\Sigma A_z$  are shown in Figs. 5a, 5b. They form a field  $A(x, z)$  making an angle  $\theta(x, z)$  with the  $z$ -axis, which gradually increases as a function of  $x$  from zero to  $\pi$  (Fig. 5c). The polarization vector  $\mathbf{P}$  will (more or less) “follow” this field. The length  $L_{\text{sim}}$  in our model (Fig. 1b) is divided in  $N$  steps of length  $dx_s$ . After each step  $k$  ( $-40/-70 + dx_s < x_k < +70/+40$ ,  $k = 1, \dots, N$ ), the precession is calculated as a matrix product with increasing number of factors:

$$P(t) = \prod_{j=1}^{j=k} R_y(\theta_j) R_z(\alpha_j) R_y^{-1}(\theta_j) P_{\text{in}} \equiv (\mathfrak{R}^k) P_{\text{in}}, \quad (9)$$

input  $\theta_j$  and  $\alpha_j$  are calculated from  $\Sigma A_x$  and  $\Sigma A_z$  and plotted in Fig. 5c:

$$\theta_j = \tan^{-1}[\Sigma A_x(x_j, z)/\Sigma A_z(x_j, z)] \quad (10)$$

(field orientation),

$$\alpha_j = (\gamma m_n/h) |A|(x_j, z) \lambda dx_s \quad (\text{precession phase}). \quad (11)$$

As input for the matrix with  $k = 1$ , we take the vectors  $[(100), (010), (001)]$ , that is, the matrix  $(\mathfrak{S})$ . The output for matrix  $(\mathfrak{R}^k)_{ij}$  ( $i, j = x, y, z$ ;  $k = 1 \dots N$ ) is shown in Fig. 4 in the  $(3 \times 3)$  layout. Third column, showing the evolution of the vector  $(001)$ , is easily interpreted: this vector “flips” almost to  $(010)$ , but the  $x$  and  $y$  components appear. To see the precession, we must prepare  $(100)$  or  $(010)$  as input (first or second column) using a polarization rotator (device R1 in Fig. 1a) ending at  $x = -40$ . Independently, using the second rotator R2 beginning at  $x = 70$ , we can select any mode in Fig. 4.

### Precession Phase

To discuss NSE, we need to know the collected precession phase  $\phi(x_k)$  along the trajectory. Following the practice of 3D polarization analysis [12], we calculate  $\phi(x_k)$ , assuming that the equipment  $\{\pi/2 - \text{rotator} + \text{anal} + \text{detec}\}$  is installed at  $x_k$  and that we measured the elements  $P_{yy} \approx \cos \phi(x_k)$  and  $P_{yx} \approx \sin \phi(x_k)$ . Here they are identified with the elements of the matrix  $(\mathfrak{R}^k)$  with  $k = 1, \dots, N$ . The phase  $\phi(x_k)$  can be found uniquely in the interval  $[-\pi, \pi]$  by calculating:

$$\phi(x_k) = \tan^{-1}[P_{yx}/P_{yy}] \equiv \tan^{-1}[(\mathfrak{R}^k)_{yx}/(\mathfrak{R}^k)_{yy}] \quad (12)$$

( $k = 1, \dots, N$ ).

The result (multiplied by 100) is shown in Fig. 7 (line 1). We made a routine to recover multiples of  $2\pi$  (line 2). To get a meaningful result,  $N$  must be chosen so high that  $\alpha_j < \pi$  for all  $j$ . In Fig. 5c, we can verify: this condition is fulfilled. This is  $\phi(x_k)$  in the rotating system. The phase in the LAB system (line 3) is obtained by adding the phase  $\varphi_{\text{RF}}(x) = \omega_{\text{RF}}(m_n/h)\lambda x$  of the ROT system (line 4).

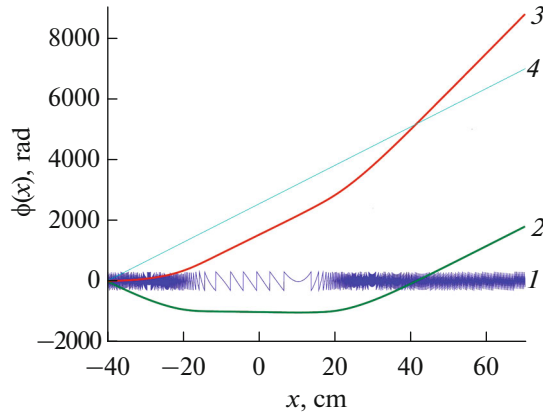


**Fig. 7.** Collected precession phase  $\phi(x)$  through F1 according to the data  $P_{yx}$  and  $P_{yy}$  in Fig. 4: (1)  $\times 100$  in the ROT system; (2) after  $\pi$ -retrieve; (3) in the LAB system; (4) the phase in the ROT system.

### Modular Simulation of Full SESANS Setup

We enter three vectors  $[(P_{xx}, P_{xy}, P_{xz}), (P_{yx}, P_{yy}, P_{yz}), (P_{zx}, P_{zy}, P_{zz})]$  at the end of F1 as input to F2. This is repeated for F3 and F4 using the same software – a modular simulation scheme:

$$\mathbf{P} = (\mathfrak{R}^N)_{F4} (\mathfrak{R}^N)_{F3} (\mathfrak{R}^N)_{F2} (\mathfrak{R}^N)_{F1} \mathbf{P}_{in}. \quad (13)$$

For each flipper, the matrix  $(\mathfrak{R}^N)$  is given by  $(\mathfrak{R}^k)$ , (10), and  $k$  runs from one to  $N$ . As the input polarization vectors in step 1 of  $(\mathfrak{R}^1)_{F1}$ , we take matrix  $(\mathfrak{S})$ . The matrix (13) is unitary:  $|\mathbf{P}|$  remains equal unity. The phase  $\phi(x_k)$  in F1 is found from Eq. (12). The precession phase through F2 is added to the phase at the end of F1, etc. The precession phase  $\phi(x)$  is shown in Fig. 8, flippers ON. Notice that after conversion to the LAB system between F1–F2 and F3–F4, the slope  $d\phi/dx \approx 2 \times$  the slope in the flippers: the polarization vector collects the precession phase, although the

magnetic field is almost zero. This is “zero field precession” [13] at a frequency of  $\approx 2\omega_{RF}$ .

### Beam of Neutrons

For a fixed  $\psi$  (Fig. 1b), we define a vertical “divergent ribbon beam”. Its trajectories starting at  $x = -40$  have slopes  $\zeta$ , so that they remain on the “ribbon”, therefore  $|z_0| < 1$  (Fig. 1c) to the end of F4 at  $x = 400$ : they will end in the detector. Thus, starting at  $z_0 = 0$ , slope  $\zeta$  must be  $< 1/440$ , i.e., in the interval  $[-2.45, +2.45$  mrad]; starting at  $z_0 = -1$  – in the interval  $[0, +4.9$  mrad], etc. These restrictions correspond to the area indicated by  $F = 1$  in Fig. 9. This is the locus of trajectories in the divergent ribbon beam. We give them the weight  $F(z_0, \zeta) = 1$ ; the other is  $F = 0$ . With the selected step, width Fig. 9 includes  $21 \times 41 = 861$  trajectories; the area  $F = 1$  contains 441 trajectories. For each of the latter, we “simulate” the precession for  $\lambda = 4 \text{ \AA}$ , applying (13). For each flipper, the product matrix  $(\mathfrak{R}^N)$  is calculated using (12) up to  $k = N$ ;  $\theta_j$ 's and  $\alpha_j$ 's depend on the parameters  $(z_0, \zeta)$ . The matrix (13) is unitary:  $|\mathbf{P}|$  remains equal unity.

For each trajectory, we calculate the final phase  $\phi$  ( $x = 400$ ), denoted  $\Phi(z, \zeta)$ , using (13), and then the module for multiples of  $2\pi$  (Fig. 9). The spin-echo is not sharp: there is a spread of 1.5 rad, mainly due to the coefficient  $\gamma_B$  in (4). Since the fields in our flippers are independent of  $y$ , the results for a divergent ribbon beam are valid also for a finite beam thickness  $\Delta y$ . Therefore, henceforth, we discard the idea of “ribbon”.

### Phase Coil Signal

The beam polarization  $P$  is the average of the  $y$ -component of the vector  $\mathbf{P}(z_0, \zeta)$  over the area  $F = 1$  (Fig. 9) obtained as a result of simulating (13):  $P \equiv \langle P_y(z_0, \zeta) \rangle_{F=1}$ . To account for the precession  $\Delta\phi$  in the

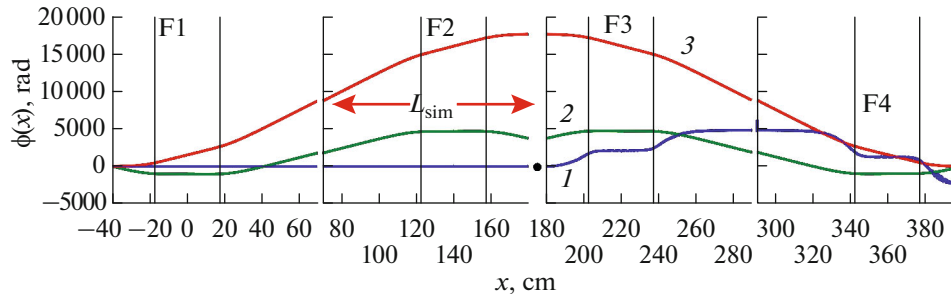


**Fig. 8.** Precession phase through the setup along a trajectory  $|x$  starting at  $x = -40$ , with  $\lambda = 4 \text{ \AA}$ ,  $RF = 1 \text{ MHz}$ ,  $z_0 = 0.5$ ,  $\psi = 0$ ,  $\zeta = 0$  in the LAB and in ROT systems. The vertical lines are the ends of the poles of the DC magnets: (1) deviation  $\Delta\phi(\times 1000)$  in precession phase for a “ray” scattered in sample (●) in the plane  $z \equiv 0$  by 0.1 mrad, i.e., the wavevector transfer  $Q_y = 1.57 \times 10^{-4} \text{ \AA}^{-1}$ ; (2) in the ROT system; (3) in the LAB system. Note: a scattering angle of only 0.1 mrad gives a precession shift  $\Delta\Phi = 2.56$  rad! This means that the poles of the DC magnets must be aligned very precisely.

phase coil (geometry is not specified: for fixed  $\lambda$ , it gives an equal phase  $\Delta\phi$  around  $z$  for all trajectories), we multiply the product matrix in (13) by  $R_z(\Delta\phi)$  for each trajectory and take the average value of the  $yy$ -element of the resulting matrices. Each matrix is considered as a “pure” rotation around  $z$  by  $\Phi(z, \zeta)$  (if the efficiency of the flippers is close to unity, in practice for  $\lambda > 3 \text{ \AA}$ ). So, the phase coil signal becomes:

$$P(\Delta\phi) \equiv \langle \cos[\Phi(z, \zeta) + \Delta\phi] \rangle_{F=1}. \quad (14)$$

To simulate a sweep with a phase coil through  $2\pi$ , we repeat this for  $\Delta\phi = i\pi/6$  ( $i = -6, \dots, 6$ ). The line 1 in Fig. 10 is the signal  $P(\Delta\phi)$  found in this way when the averaging is limited to  $\zeta = 0$ : the amplitude is unity. When averaging over the entire area  $F = 1$ , it drops to 0.92.

## SESANS: SCATTERING IN SAMPLE

### Divergent Beam at $\psi \neq 0$

From the map  $B_z^{\text{DC}}(x, y)$  of 33°-poles, we know that the labeling coefficient  $\Gamma$  in (1) is constant in the region  $\Delta y$  of more than 20 mm. Then we can compose the field profile  $B_z(x, z_0, \psi \neq 0)$  using a flipper along a trajectory with  $\zeta = 0$ , but at an angle  $\psi \neq 0$  from the profiles along the axis, as shown for F1 in Fig. 2.  $B_z(x, z_0, \psi \neq 0)$  for flipper with number  $j$  from:

$$B_{1,z}^j(x, z_0) \equiv B_z^{\text{DC}}(x + dx_{1,j,\psi}) \quad (15)$$

(profile along line 1),

$$B_{2,z}^j(x, z_0) \equiv B_z^{\text{DC}}(x + dx_{2,j,\psi}) \quad (16)$$

(profile along line 2),

with the  $x$  shifts,  $dx_{1,j,\psi} = (j-1)\psi L_{\text{sim}} \cot\theta_0$  and  $dx_{2,j,\psi} = j\psi L_{\text{sim}} \cot\theta_0$ , shown in Fig. 1b for flipper F2:  $j=2$ . The profile  $B_z(x, z_0, \psi \neq 0)$  represents the transition from (15) to (16), described by the parameter  $\varepsilon(x)$ , which runs linearly from zero to one along the length  $L_{\text{sim}}$  (Fig. 1b):

$$B_z^j(x, z_0, \psi) = (1 - \varepsilon)B_{1,z}^j(x, z_0) + \varepsilon B_{2,z}^j(x, z_0). \quad (17)$$

This equation is also valid trajectories with a slope  $\zeta \neq 0$ , including correction (4).

### Angle $\psi$ in NSE-Arm 1 Different from Arm 2: Scattering

When we insert the profiles  $B_z^j(x, z_0, \psi)$  in (13) with  $\psi$  in the F3–F4 flippers other than  $\psi$  in F1–F2, we simulate the scattering in the sample between F2 and F3. Taking 0.1 mrad for this difference gives the final offset  $\Delta\Phi(x=400) = 2.56$  (Fig. 8). Then we can calculate the coefficient  $\Gamma$  using (2),  $\Gamma = \Delta\Phi(\lambda\theta_s)$  is rewritten. In other words, (2) becomes the conversion  $\lambda \rightarrow \delta$ :

$$\delta(\lambda) = \Gamma / (2\pi)\lambda^2 \quad (1 \text{ MHz: } \Gamma = 0.64 \times 10^4 \text{ \AA}^{-1}, \quad (18)$$

$$1.5 \text{ MHz: } \Gamma = 0.99 \times 10^4 \text{ \AA}^{-1}).$$

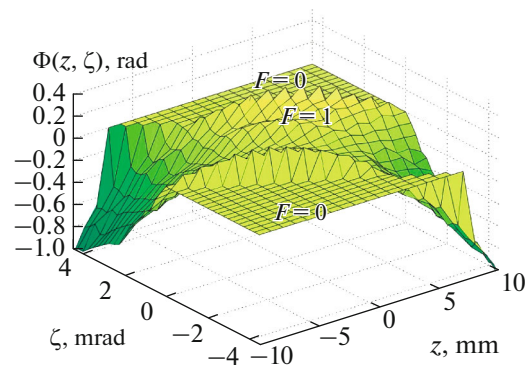


Fig. 9. The final precession phase  $\Phi(z, \zeta)$  through the full setup along the trajectories ( $\lambda = 4 \text{ \AA}$ ).

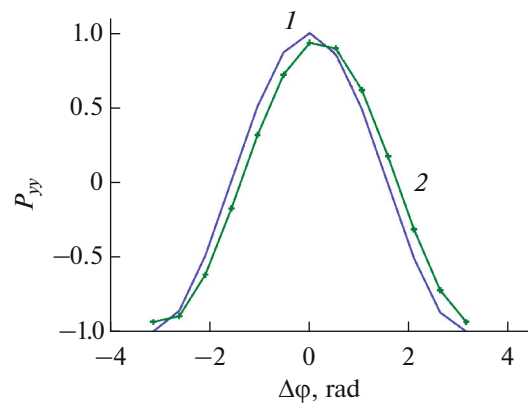


Fig. 10. The phase coil signal  $P_{yy}(\Delta\phi)$  obtained using (14) at  $\lambda = 4 \text{ \AA}$  (contrary to practice, it does not fade, because the simulation has no  $\lambda$  spread): (1) the averaging is limited to  $\zeta = 0$ ; (2) the averaging is over the entire area.

We simulated (13) for  $\lambda = 2\text{--}10 \text{ \AA}$ . The amplitudes  $P_0(\lambda)$  in (13) are shown in Fig. 11a. Then  $P_0(\lambda)$  is less than for 1 MHz, because (4) gives a stronger correction for a higher DC field. Figure 11 shows the calibration of the empty beam  $P_0(\lambda)$  and  $P_0(\delta)$  for a beam 2 cm high.

## DISCUSSION

### Polarization Rotators

Using the identity matrix ( $\mathfrak{S}$ ) as input, we assume that polarization rotator R1 (Fig. 1a) precisely “sets” the polarization vector along  $x$ ,  $y$ , and  $z$ . In reality, R1, receiving polarization (001), creates vectors that make up the  $(3 \times 3)$  matrix, denoted by  $\mathfrak{P}_1$ , deviating from  $\mathfrak{S}$ . R1 contains two longitudinal coils for setting  $x$  and a “V-coil” for each of the  $y$  and  $z$  settings. In Fig. 1a, the V-coil for setting  $y$  is shown schematically. For all three settings, we simulated the precession in R1 for  $\lambda = 4 \text{ \AA}$  (with the matrix  $\mathfrak{S}$  as input, in a fixed coordinate system) in a manner analogous to (7)–(11). The

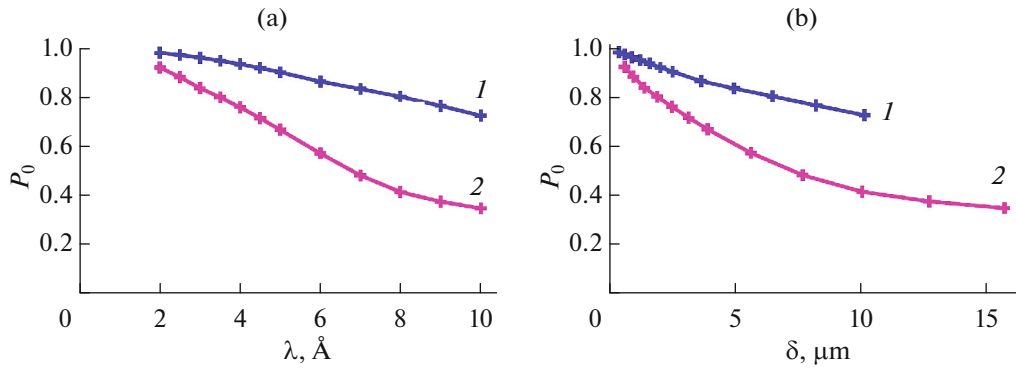


**Fig. 11.** Prediction of the  $P_0(\lambda)$  calibration for the setup in Fig. 1b with a net length 4.4 m for a divergent beam 2 cm high at the radio frequency (1) 1 and (2) 1.5 MHz: (a) as a function of  $\lambda$ ; (b) after converting  $\lambda$  to  $\delta$  using (18).

result is three matrices; their third columns are combined to:

$$\mathbf{P}_1 = [(0.983, -0.166, -0.080), (0.018, 0.955, 0.296), (001)], \quad (19)$$

instead of  $\mathfrak{S}$ . This matrix is no longer unitary: its determinant is 0.942, which we consider as satisfactory. Rotator R2 “freezes” the polarization matrix at  $x = 400$  and “transports” it in the  $z$  direction of the analyzer field. This is described using the matrix  $\mathbf{P}_2$  inverse to  $\mathbf{P}_1$ . Thus, taking into account the rotators R1 and R2, the product matrix  $\mathfrak{H}^k$  in (14) becomes equal to  $\mathbf{P}_2(\mathfrak{H}^k)\mathbf{P}_1$ . Equation (19) shows that  $\mathbf{P}_1$  and  $\mathbf{P}_2$  do not deviate too much from  $\mathfrak{S}$ ; moreover, reversing the precession between F2 and F3, they hardly affect the final phases  $\Phi(z, \zeta)$ . Therefore we ignored them.

#### Polarization $P_0(\lambda)$

There are two reasons why  $P_0$  drops along the beam through the flippers F1–F4. The first reason is that the polarization component appears in the  $xy$  plane, since the angle  $\theta(x)$  does not reach  $\pi$  (Fig. 5c). This is valid for each trajectory. Moreover, for many trajectories this component grows in successive flippers; it can be reduced by increasing the DC gradient. The second reason is that, as a result of the correction  $\gamma_B$  (4), the field increases with  $z^2$  from the beam axis to magnet poles. This fact, characteristic of the design of our DC magnets, is the main reason for spread in the final phase  $\Phi(z, \zeta)$  (Fig. 8), it is crucial for maximum beam height. This spread is largely nullified within each DC magnet by spin flipping. If the RF and gradient fields are “OFF”, the spread is so great that the amplitudes of the phase coil signals drop below 0.2 even for  $\lambda = 2$  Å.

#### Ribbon Beam

There was criticism of the concept of a vertical ribbon beam. Due to the independence of the fields of  $y$ ,

the ribbon can be expanded to a beam of finite width of the order of 1 cm. If we know details of the neutron guide supplying SESANS, we could introduce a more realistic beam.

## CONCLUSIONS

The routines developed here are ways of simulating the Larmor precession in a rather complex magnetic field configuration for neutron paths at angles  $(\zeta, \psi) \neq 0$  relative to the beam axis. The values of  $\delta$  (Fig. 11) leave much to be desired; we could increase  $\delta$  by placing the flippers in each NSE-arm farther apart, due to loss of intensity. As shown in [14], radio frequencies of 2–3 MHz are possible. They give realistic forecast for achieving  $\delta = 20$   $\mu\text{m}$ . The routines can be used for studying deviations of parameter settings from design ones. We calculated the precession phases not just by calculating the field integrals, but by stepwise matrix multiplication.

## FUNDING

This work is supported by the Russian Science Foundation (grant no. 19-12-00363).

## REFERENCES

1. M. Th. Rekveldt, J. Plomp, W. G. Bouwman, W. H. Kraan, S. V. Grigoriev, and M. Blaauw, *Rev. Sci. Instrum.* **76**, 03390 (2005).
2. T. Krouglov, W. G. Bouwman, J. Plomp, M. Th. Rekveldt, G. J. Vroege, A. V. Petukhov, and D. M. E. Thies-Weesie, *J. Appl. Crystallogr.* **36**, 1417 (2003).
3. R. Andersson, L. F. van Heijkamp, I. M. de Schepper, and W. G. Bouwman, *J. Appl. Crystallogr.* **41**, 868 (2008).
4. E. G. Iashina, E. V. Velichko, M. V. Filatov, W. G. Bouwman, C. P. Duif, A. Brulet, and S. V. Grigoriev, *Phys. Rev. E* **96**, 012411 (2017).

5. E. G. Iashina, M. V. Filatov, R. A. Pantina, E. Y. Varfolomeeva, W. G. Bouwman, C. P. Duif, D. Honecker, V. Pipich, and S. V. Grigoriev, *J. Appl. Crystallogr.* **52**, 844 (2019).
6. S. V. Grigoriev, Th. M. Rekveldt, T. V. Krouglov, W. H. Kraan, and W. G. Bouwman, *J. Appl. Crystallogr.* **39**, 252 (2006).
7. S. V. Grigoriev, Y. Chetverikov, V. Zabenkin, W. H. Kraan, Th. M. Rekveldt, and N. van Dijk, *J. Appl. Crystallogr.* **40**, 111 (2007).
8. E. G. Iashina, W. G. Bouwman, C. P. Duif, M. V. Filatov, and S. V. Grigoriev, *J. Phys.: Conf. Ser.* **862**, 012010 (2017).
9. W. H. Kraan, V. N. Zabenkin, L. A. Axelrod, Y. O. Chetverikov, S. V. Grigoriev, E. G. Iashina, and A. A. Sumbatyan, *J. Surf. Invest.: X-ray, Synchrotron Neutron Tech.* **11**, 1282 (2017).
10. A. Abragam, *Principles of Nuclear Magnetism* (Oxford University Press, New York, 1961), p. 599.
11. S. V. Grigoriev, A. I. Okorokov, and V. V. Runov, *Nucl. Instrum. Methods Phys. Res., Sect. A* **384**, 451(1997).
12. M. Th. Rekveldt, *Z. Phys.* **259**, 390 (1973).
13. R. Golub and R. Gähler, *Phys. Lett. A* **123**, 43 (1987).
14. A. A. Sumbatyan, RF Patent No. 172332 U1 (9 January 2017).